International Journal of Minerals, Metallurgy and Materials
Volume 30, Number 3, March 2023, Page 581
https://doi.org/10.1007/s12613-022-2556-7

Constructing $BaTiO_3/TiO_2$@polypyrrole composites with hollow multishelled structure for enhanced electromagnetic wave absorbing properties

Dan Mao[1,3], *Zhen Zhang*[2], *Mei Yang*[1),✉], *Zumin Wang*[1], *Ranbo Yu*[2),✉], *and Dan Wang*[1,3),✉]

1) State Key Laboratory of Biochemical Engineering, Institute of Process Engineering, Chinese Academy of Sciences, Beijing 100190, China
2) Department of Energy Storage Science and Engineering, School of Metallurgical and Ecological Engineering, University of Science and Technology Beijing, Beijing 100083, China
3) University of Chinese Academy of Sciences, Beijing 100049, China
(Received: 9 June 2022; revised: 22 September 2022; accepted: 27 September 2022)

Abstract: $BaTiO_3/TiO_2$@polypyrrole (PPy) composites with hollow multishelled structure (HoMS) were constructed to enhance the electromagnetic wave absorbing properties of $BaTiO_3$-based absorbing material. $BaTiO_3/TiO_2$ HoMSs were prepared by hydrothermal crystallization using TiO_2 HoMSs as template. Then, $FeCl_3$ was introduced to initiate the oxidative polymerization of pyrrole monomer, forming $BaTiO_3/TiO_2$@PPy HoMSs successfully. The electromagnetic wave absorbing properties of $BaTiO_3/TiO_2$ HoMSs and $BaTiO_3/TiO_2$@PPy HoMSs with different shell number were investigated using a vector network analyzer. The results indicate that $BaTiO_3/TiO_2$@PPy HoMSs exhibit improved microwave absorption compared with $BaTiO_3/TiO_2$ HoMSs. In particular, tripled-shelled $BaTiO_3/TiO_2$@PPy HoMS has the most excellent absorbing performance. The best reflection loss can reach up to −21.80 dB at 13.34 GHz with a corresponding absorber thickness of only 1.3 mm, and the qualified absorption bandwidth of tripled-shelled $BaTiO_3/TiO_2$@PPy HoMS is up to 4.2 GHz. This work paves a new way for the development of high-performance composite microwave absorbing materials.

Keywords: $BaTiO_3/TiO_2$@polypyrrole composites; hollow multishelled structure; electromagnetic wave absorbing

1. Introduction

The rapid development of electronic devices has brought progressively serious electromagnetic pollution, which poses a considerable threat to physical health and information security [1–2]. Electromagnetic shielding materials and electromagnetic wave (EMW) absorbing materials have been widely applied to solve the electromagnetic pollution. Electromagnetic shielding materials limit EMW by physical reflection, which may cause secondary pollution. EMW absorbing materials dissipate EMW through energy conversion, which can reduce the possibility of secondary pollution. Therefore, EMW absorbing materials receive more attention in the past few decades because of their environmental friendliness and high efficiency [3–5].

EMW absorbing materials can be divided into magnetic materials, dielectric materials, and conductive materials according to their different mechanisms for EMW absorption. However, the magnetic materials are characterized by high density, susceptibility to corrosion, and low Curie temperature, which limits their application to a certain extent [6–7]. Recently, binary dielectric composites have received extensive attention for their efficient and stable EMW absorbing properties [8–9]. For example, Cui *et al.* [10] synthesized the binary dielectric $BaTiO_3$@C core–shell material. The results showed that composite material has an amazing minimum reflection loss (RL) of −88.5 dB. Wang *et al.* [11] synthesized hollow cube-like $ZnSnO_3$ wrapped by multi-walled carbon nanotubes (MWCNTs) and studied the EMW absorbing properties of $ZnSnO_3$@MWCNTs material. The results showed that the minimum RL reaches −52.1 dB and the effective absorption bandwidth (EAB) is up to 3.9 GHz. Mu *et al.* [12] prepared $La_{1-x}Sr_xMn_{1-y}Fe_yO_3$ nanostructures with different doping sites by the solid phase reaction method, and then mixed them with $2MgO\cdot 2Al_2O_3\cdot 5SiO_2$ (MAS). The results showed that $La_{0.7}Sr_{0.3}Mn_{0.8}Fe_{0.2}O_3$/MAS can achieve the widest bandwidth of 4.2 GHz covered the entire X-band (8.2–12.4 GHz) and a minimum RL value of −17.99 dB at 500°C, which has a great prospect as an efficient high temperature microwave absorber.

The optimization of the structure represents one of the significant means to improve the EMW absorbing properties of materials. Hollow multishelled structure (HoMS) has the characteristics of low density, large specific surface area, high loading capacity, as well as multiple scattering of incident light or waves. More importantly, size, composition, and shape of HoMSs, as well as shell number, shell thickness, and intershell space, can be flexibly designed and adjusted

✉ Corresponding authors: Mei Yang E-mail: myang@ipe.ac.cn; Ranbo Yu E-mail: ranboyu@ustb.edu.cn; Dan Wang E-mail: danwang@ipe.ac.cn

according to the requirements of application. It can be inferred that HoMSs with multiple shells and rich interfaces will have unique advantages as EMW absorbing materials [13–15]. For example, Yang *et al.* [16] proved that the EMW absorbing performance of C@MnO_2 HoMSs is far superior to the mixed materials of hollow C spheres and MnO_2. Liu *et al.* [17] verified that the EMW absorbing performance of double-shell (2s)-Fe_3O_4@SnO_2 HoMSs is much better than single-shell (1s)-Fe_3O_4@SnO_2. Tao *et al.* [18] proved that the three-shell porous carbon HoMS has the best EMW absorbing performance.

As a dielectric material, barium titanate not only has a high dielectric constant, but also has advantages in ferroelectric activity, nonlinear optical coefficient, and spontaneous polarization. In particular, spontaneous polarization generated by Ti^{4+} shifting and oxygen octahedron distorting will induce dielectric relaxation in the gigahertz frequency bands, which contributes to the dielectric loss of incident EMW [19–21]. For example, Zhu *et al.* [22] grew a layer of $BaTiO_3$ on MWCNTs by sol–gel method. The composite showed better EMW absorption performance compared to MWCNTs, with a minimum RL of −25.7 dB and EAB up to 5.8 GHz.

Besides, the conductive polymer is another type of EMW absorbing material based on conductance loss. In general, conductive polymers have conjugated π bond, and under the action of an external electromagnetic field, π electrons will move directionally to form a conductive network to consume the incident EMW [23–24]. For example, Pang *et al.* [25] successfully synthesized polyethylene dioxythiophene (PEDOT) HoMSs using Fe_3O_4 as a sacrificial template. Compared with PEDOT solid spheres or single- and double-shell hollow spheres, triple-shell (3s)-PEDOT exhibits better absorption performance, with a minimum RL of −39.7 dB, an EAB of about 4.6 GHz, and a matching thickness of only 2 mm.

Multi-components EMW absorbing materials with different attenuation mechanisms can help to improve the absorbing properties. Especially, HoMS exhibits obvious advantages, such as large specific surface area, effective absorption of EMW, and interfacial polarization. Therefore, we believe that coating the conducting polymer, polypyrrole (PPy), on the surface of dielectric material $BaTiO_3$/TiO_2 HoMS is a novel and effective path to improve the absorbing properties of EMW absorbing materials. In this work, we propose a strategy for constructing $BaTiO_3$/TiO_2@PPy HoMSs by *in-situ* hydrothermal crystallization and pyrrole monomer evaporation using TiO_2 HoMSs as the template. The $BaTiO_3$/TiO_2@PPy HoMSs exhibit improved microwave absorption compared with $BaTiO_3$/TiO_2 HoMSs, which is better than those of most binary dielectric $BaTiO_3$-based composites.

2. Experimental

2.1. Chemicals

All reagents, including sucrose, titanium tetrachloride ($TiCl_4$), barium hydroxide octahydrate ($Ba(OH)_2·8H_2O$), tetrabutylammonium hydroxide (25wt%), hydrochloric acid, hydrated ferric chloride ($FeCl_3·6H_2O$), and pyrrole monomer, were purchased from Beijing Chemical Reagent Company, China. All chemicals were of analytical grade and used without further purification. Deionized water (Millipore Milli-Q grade) with a resistivity of 18.2 MΩ·cm was used in all the experiments.

2.2. Preparation

2.2.1. Preparation of $BaTiO_3$/TiO_2 HoMSs

TiO_2 HoMSs were prepared via a sequential templating approach according to previous work [26]. Carbonaceous microspheres were dispersed in 3 M $TiCl_4$ aqueous solution, 1s-, 2s-, and 3s-TiO_2 hollow spheres can be produced by controlling the adsorption time and calcination procedure. The preparation of 1s-$BaTiO_3$/TiO_2 HoMSs is taken as an example. Firstly, 157.7 mg $Ba(OH)_2·8H_2O$ and 40 mg 1s-TiO_2 were added to 19 mL deionized water. After ultrasonic treatment for 15 min, 1 mL tetrabutylammonium hydroxide solution (25wt%) was added and transferred to a sealed Teflon stainless-steel autoclave. After heating at 145°C for 4.5 h, the obtained products were washed by 1 M HCl solution, deionized water, and dried at 60°C for 12 h. The preparation process of 2s- and 3s-$BaTiO_3$/TiO_2 HoMSs was similar to that of 1s-$BaTiO_3$/TiO_2 HoMSs.

2.2.2. Preparation of $BaTiO_3$/TiO_2@PPy HoMSs

Taking preparation of 1s-$BaTiO_3$/TiO_2@PPy HoMSs as an example, firstly, 90 mg 1s-$BaTiO_3$/TiO_2 HoMSs were added to 300 μL of 0.5 M $FeCl_3·6H_2O$ solution under continuous stirring at 40°C in a small beaker until the solution completely evaporated, secondly, pyrrole monomer was put into another small beaker, and the two beakers were sealed together and placed in an oven at 50°C for 24 h. The oxidative polymerization of the pyrrole monomer was conducted, and the final black powder was termed as 1s-$BaTiO_3$/TiO_2@PPy HoMS. The preparation process of 2s- and 3s-$BaTiO_3$/TiO_2@PPy HoMSs was similar to that of 1s-$BaTiO_3$/TiO_2@PPy HoMSs.

2.3. Characterization

Powder X-ray diffraction (XRD) patterns were recorded on a Panaltical X'Pert-pro MPD X-ray powder diffractometer using Cu K_α radiation (λ = 0.15405 nm). Scanning electron microscope (SEM) was performed on a JEOL JSM-6700 scanning electron microscope. Transmission electron microscope (TEM) was performed on FEI Tecnai F20 electron microscope operated at 200 kV. X-ray photoelectron spectroscopy (XPS) spectra were recorded using Thermo Scientific K-Alpha+ system. Raman spectra were recorded on a Jobin Yvon T64000 spectrograph at room temperature. Fourier transform infrared spectroscopy (FTIR) spectra were obtained by Fourier transform infrared spectrometer of Nicolet Company.

The relative complex permittivity and permeability in the frequency range from 1 to 18 GHz were obtained by the coaxial reflection/transmission method using a vector network analyzer (VNA, PNA-E5071C). A sample containing 70wt% of $BaTiO_3/TiO_2$ HoMSs or $BaTiO_3/TiO_2$@PPy HoMSs was pressed into a ring with an inner diameter of 3.04 mm, an outer diameter of 7.0 mm, and a thickness of 2.0 mm for microwave measurement, in which paraffin wax was used as the binder.

3. Results and discussion

3.1. Phase and morphology characterization

The preparative strategy for $BaTiO_3/TiO_2$@PPy HoMSs is schematically depicted in Fig. 1. Carbonaceous microspheres (CMS) were chosen as the initial template for synthesis TiO_2 HoMSs by sequential templating approach. After hydrothermal reacting the TiO_2 HoMSs with $Ba(OH)_2$ solutions for 4.5 h, the TiO_2 HoMSs changed to $BaTiO_3/TiO_2$ HoMSs. Finally, $BaTiO_3/TiO_2$@PPy HoMSs were prepared by introducing $FeCl_3$ to trigger the oxidative polymerization of pyrrole monomer.

XRD patterns of $BaTiO_3/TiO_2$ and $BaTiO_3/TiO_2$@PPy HoMSs are shown in Fig. 2(a). All the detected diffraction peaks can be indexed in the cubic structure of $BaTiO_3$ (JCPDS No. 31-0174). It can be seen that there are weak TiO_2 characteristic peaks of the anatase phase (JCPDS No. 21-1272) and rutile phase (JCPDS No. 21-1276), which is attributed to the residual TiO_2 in the hydrothermal crystallization of $BaTiO_3$. The composite with multi-component may enhance the loss of EMW due to multiple effective interfaces and increased defect polarization. There are no obvious characteristic peaks of PPy in XRD patterns, which may be due to the thin coating of PPy on the surface of $BaTiO_3/TiO_2$ HoMSs.

The FTIR spectra of 2s-TiO_2, 2s-$BaTiO_3/TiO_2$, and 2s-$BaTiO_3/TiO_2$@PPy HoMSs are displayed in Fig. 2(b). For 2s-TiO_2 and 2s-$BaTiO_3/TiO_2$ HoMSs, a characteristic peak at 520 cm^{-1} is assigned to the Ti–O bond stretching [27]. The formation of PPy is evidenced by the characteristic peaks of the fundamental vibrations of the pyrrole ring (1548 cm^{-1}), the C–N deformation vibrations in the ring (1471 cm^{-1}), the C–H and N–H in-plane deformation vibrations (1180 cm^{-1}), and the C–H out-of-plane deformation vibrations of the ring (908 cm^{-1}), which can be observed in 2s-$BaTiO_3/TiO_2$@PPy HoMSs [24,28]. It should be noted that these characteristic peaks are all shifted by 10–20 cm^{-1} compared to the standard PPy spectrum, which may be due to interaction between $BaTiO_3/TiO_2$ and PPy.

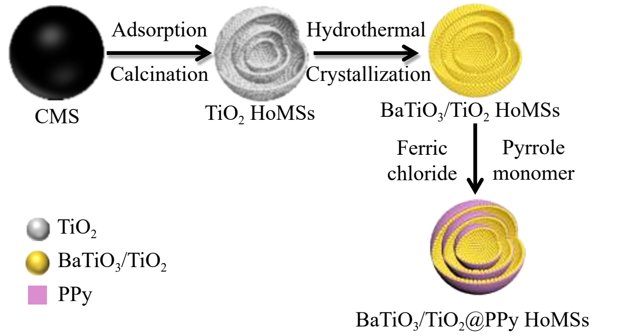

Fig. 1. Schematic illustration for the preparation of $BaTiO_3/TiO_2$@PPy HoMSs.

The Raman spectra of 2s-TiO_2, 2s-$BaTiO_3/TiO_2$, and 2s-$BaTiO_3/TiO_2$@PPy HoMSs are shown in Fig. 2(c) to further determine the crystal phase of $BaTiO_3$ in the composite. Cubic $BaTiO_3$ has no Raman activity due to its high symmetry, while the non-centrosymmetric tetragonal $BaTiO_3$ has a strong Raman peak [29–30]. The Raman spectrum of 2s-$BaTiO_3/TiO_2$ HoMSs has no obvious peaks except the characteristic peaks of TiO_2, which indicates that the synthesized $BaTiO_3$ has a cubic structure. Furthermore, the intensity of characteristic peaks of TiO_2 decrease significantly compared to 2s-TiO_2 HoMSs, which is due to the low content of TiO_2 in 2s-$BaTiO_3/TiO_2$ HoMSs. For 2s-$BaTiO_3/TiO_2$@PPy HoMSs, the intensity of the characteristic peaks of TiO_2 decrease further, which is due to the coating of PPy on the surface of 2s-$BaTiO_3/TiO_2$ HoMSs.

XPS spectrum was used to analyze the component and the chemical bond structure of the $BaTiO_3/TiO_2$@PPy HoMSs. Fig. 3 shows XPS spectrum of the 2s-$BaTiO_3/TiO_2$@PPy HoMSs and high-resolution XPS spectra of the N 1s, Ba 3d, and Ti 2p. As shown in Fig. 3(a), the surface contains C, N, O, Ba, Ti, Fe, and Cl, and Fe together with Cl should be ascribed by the iron chloride oxidant during the coating process of PPy. Fig. 3(b)–(d) represents the high-resolution XPS spectra of N 1s, Ba 3d, and Ti 2p, respectively. The N 1s peak in the XPS spectra can be reasonably deconvoluted to three-component peaks with binding energies of 398.2 eV, 399.8 eV, and 401.3 eV (Fig. 3(b)), which are attributed to imine nitrogen (–N=), amine nitrogen (–NH–), and nitrogen cationic radical (–N^+–), respectively [23]. The presence of these peaks proves the formation of PPy. The binding energies of Ba $3d_{5/2}$, Ba $3d_{3/2}$, Ti $2p_{3/2}$, and Ti $2p_{1/2}$ of the composites were

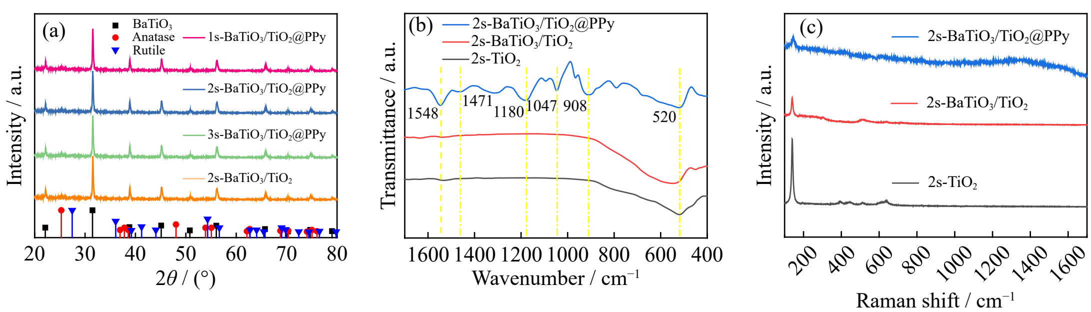

Fig. 2. (a) XRD patterns, (b) FTIR spectra, and (c) Raman spectra of 2s-TiO_2, 2s-$BaTiO_3/TiO_2$, and 2s-$BaTiO_3/TiO_2$@PPy HoMSs.

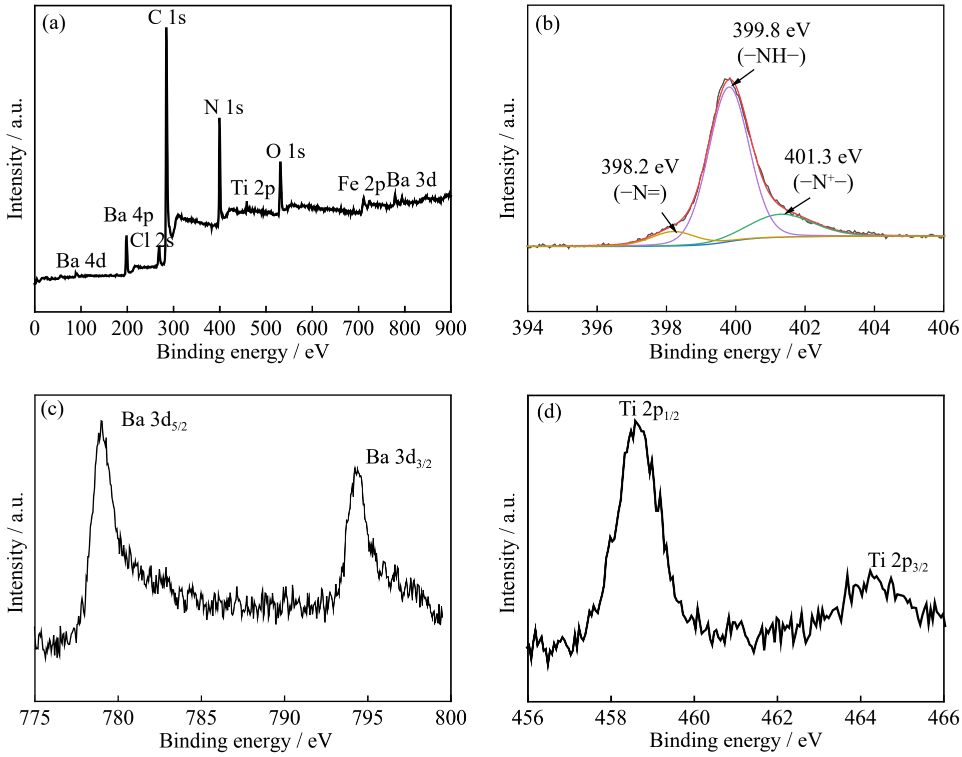

Fig. 3. (a) XPS spectra of 2s-$BaTiO_3/TiO_2$@PPy HoMSs; high-resolution XPS spectra of the (b) N 1s, (c) Ba 3d, and(d) Ti 2p.

measured to be 778.9 eV, 794.2 eV, 464.2 eV, and 458.6 eV, respectively (Fig. 3(c)–(d)), which are in good agreement with those reports [25,31–32].

Morphological characteristics of $BaTiO_3/TiO_2$@PPy were further revealed by TEM and SEM. From TEM images of $BaTiO_3/TiO_2$ HoMSs (Fig. 4(a)–(c)), we can see that the material maintains the morphology of TiO_2 HoMSs, but the crystal grain has been further enlarged. Grain size of TiO_2 HoMSs calculated by Scherer formula is 15.3 nm (Fig. S1), while the grain size of $BaTiO_3/TiO_2$ HoMSs is 47.3 nm. The broken 3s-$BaTiO_3/TiO_2$ HoMSs image can further prove that the sample has a hollow multishelled structure (Fig. 4(d)). Fig. 4(e)–(g) shows the TEM images of 1s-, 2s-, and 3s-$BaTiO_3/TiO_2$@PPy HoMSs respectively. It can be seen that the morphology remains relatively intact, and the outer shell is wrapped with a layer of PPy with a thickness of 10–30 nm. From the SEM image (Fig. 4(h)) of 3s-$BaTiO_3/TiO_2$@PPy HoMSs, it can be seen that the surface of hollow spheres changes from smooth to rough, and PPy forms a conductive network between the hollow spheres, which may enhance the EMW absorption performance. Through the TEM mapping images of 3s-$BaTiO_3/TiO_2$@PPy HoMSs (Fig. 4(i)–(j), Fig. S2), Ba, Ti, O, and N elements are evenly distributed, which proves the successful coating of PPy on the inner and outer shells of HoMSs. Furthermore, obvious lattice fringes and diffraction wreaths can be seen from high resolution transmission electron microscope (HRTEM) and selected area electron diffraction (SAED) images of 3s-$BaTiO_3/TiO_2$@PPy HoMSs (Fig. 4(k)–(l)). Among them, 0.285 nm and 0.352 nm correspond to the (110) crystal surface of $BaTiO_3$ and the (101) crystal surface of anatase respectively, which further proves the successful synthesis of $BaTiO_3/TiO_2$. The SAED image of 3s-$BaTiO_3/TiO_2$@PPy HoMSs shows a series of concentric rings with different radii, indicating that the sample has a polycrystalline structure. The red rings correspond to the (310), (211), and (110) crystal surface of $BaTiO_3$, and the yellow rings correspond to the (301), (103), and (110) crystal surface of TiO_2, respectively.

3.2. Microwave absorption performance

It is a known fact that electromagnetic parameters are significant parameters to evaluate EMW absorption performance. In general, the real part of the relative complex permittivity (ε') represents the storage capacity of the electric field energy, and the imaginary part (ε'') represents the loss capacity of the electric field energy; the real part of the relative magnetic permeability (μ') represents the storage capacity of the magnetic field energy, and the imaginary part (μ'') represents the loss capacity of the magnetic field energy [33–35]. Fig. 5(a)–(b) shows the frequency dependence of ε' and ε'' of $BaTiO_3/TiO_2$@PPy HoMSs. The ε' values of 1s-, 2s-, and 3s-$BaTiO_3/TiO_2$@PPy decrease from 33.5, 26, and 25.3 to about 13.3, respectively. This phenomenon is generally referred to the frequency diffusion characteristics and mainly due to the increased polarization hysteresis caused by high-frequency electric field variations. Similarly, ε'' also appears in the same trend, accompanied by some resonance peaks, indicating that multiple polarizations and relaxation occur under alternating electromagnetic fields. Compared with the ε' and ε'' of $BaTiO_3/TiO_2$ HoMSs (Fig. S3), the ε' and ε'' of $BaTiO_3/TiO_2$@PPy HoMSs have been greatly increased, which is mainly because PPy improves the conductivity of the composite material. Besides, 1s-$BaTiO_3/TiO_2$@PPy HoMSs have the largest ε' and ε'' in the entire frequency range, indicating that 1s-Ba-

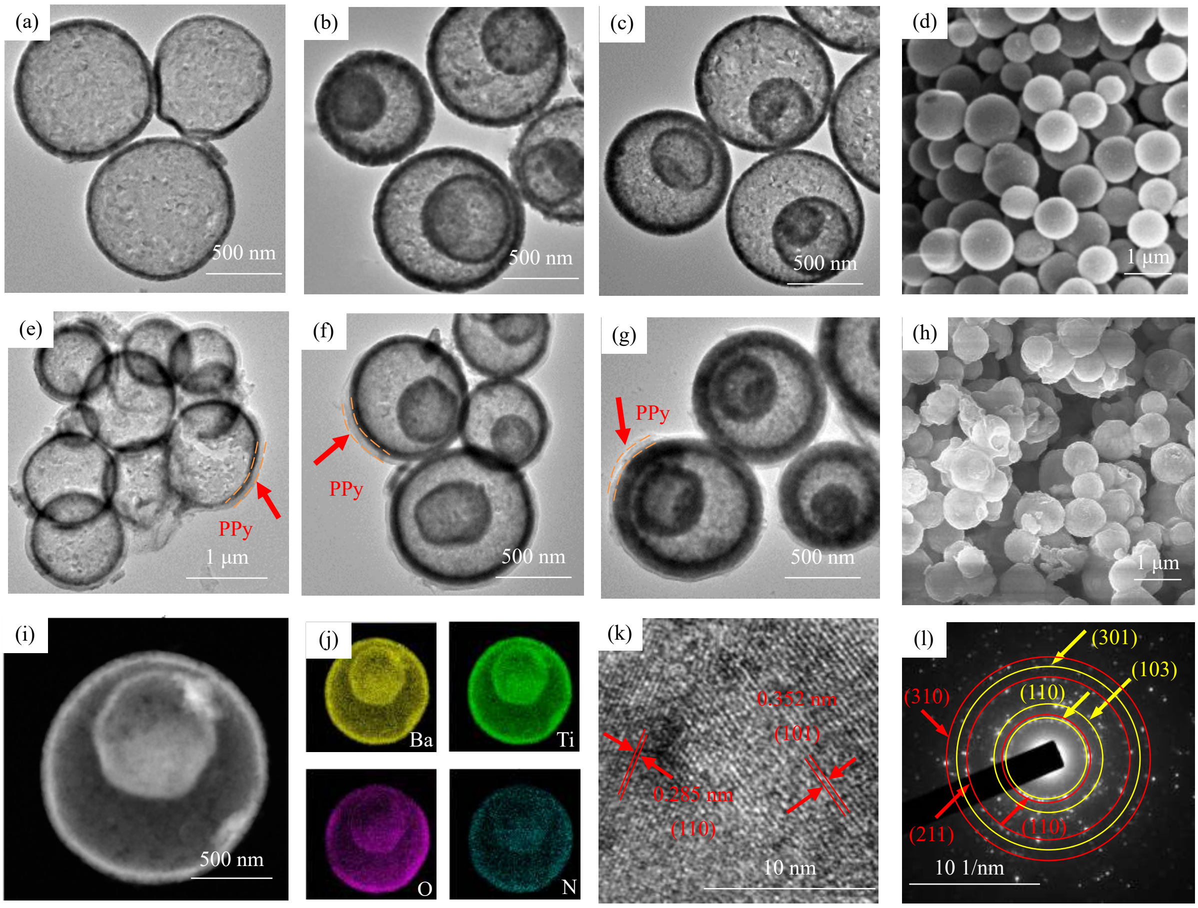

Fig. 4. TEM images of (a) 1s-$BaTiO_3/TiO_2$ HoMSs, (b) 2s-$BaTiO_3/TiO_2$ HoMSs, and (c) 3s-$BaTiO_3/TiO_2$ HoMSs; (d) SEM image of 3s-$BaTiO_3/TiO_2$ HoMSs; TEM images of (e) 1s-$BaTiO_3/TiO_2$@PPy HoMSs, (f) 2s-$BaTiO_3/TiO_2$@PPy HoMSs, and (g) 3s-$BaTiO_3/TiO_2$@PPy HoMSs; (h) SEM image of 3s-$BaTiO_3/TiO_2$@PPy HoMSs; (i, j) TEM mapping images of 3s-$BaTiO_3/TiO_2$@PPy HoMSs; (k) HRTEM and (l) SAED images of 3s-$BaTiO_3/TiO_2$@PPy HoMSs.

TiO_3/TiO_2@PPy HoMSs have the strongest electric energy storage and electric loss. The tangent value of the dielectric loss ($\tan\delta_e$) is one of the important parameters for evaluating the dielectric loss of materials. Fig. 5(c) represents the dielectric loss tangents of $BaTiO_3/TiO_2$@PPy HoMSs with frequency. The $\tan\delta_e$ of 1s-$BaTiO_3/TiO_2$@PPy HoMSs is the

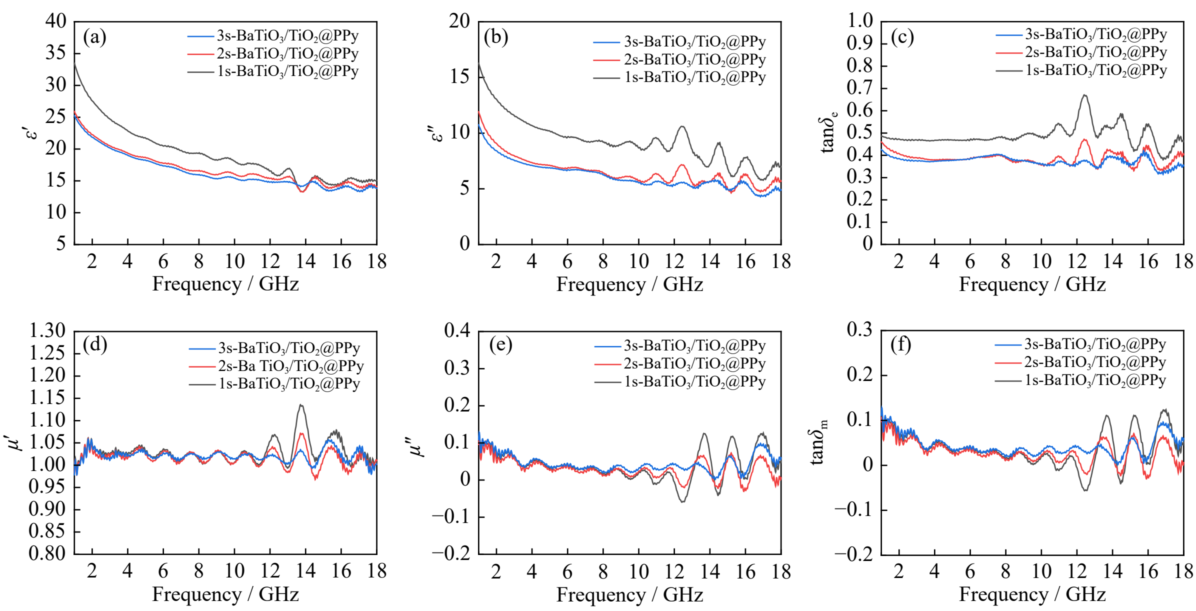

Fig. 5. (a) Real (ε') and (b) imaginary (ε'') of relative complex permittivity and (c) $\tan\delta_e$ versus frequency of $BaTiO_3/TiO_2$@PPy HoMSs; the (d) real (ε') and (e) imaginary (ε'') of relative permeability and (f) magnetic loss tangent ($\tan\delta_m$) versus frequency of $BaTiO_3/TiO_2$@PPy HoMSs.

largest in the entire frequency range, which is consistent with the result of the relative complex permittivity.

Magnetic loss is also a large part of EMW loss. For non-magnetic $BaTiO_3/TiO_2$ and PPy materials, there is no magnetic loss in theory. However, these materials may have weak magnetic loss due to quantum size effect, macroscopic quantum tunneling effect, small size and interface effect, or the addition of weak Fe oxidant. Fig. 5(d)–(f) shows that there are weak magnetic losses in the high frequency range, but they are almost negligible compared to the dielectric loss.

The dielectric loss of materials includes polarization loss and conduction loss. For polarization loss, since the formation time of electron displacement polarization and ion displacement polarization is very short, they have no visible effect on the complex permittivity. Therefore, only interfacial polarization, dipole polarization, and thermal ion relaxation polarization need to be considered in the microwave band [36]. Dipole polarization and thermal ion relaxation polarization can generate relaxation behavior and lead to polarization loss. According to the Debye relaxation polarization theory, when polarization relaxation occurs, there will be a Cole–Cole semicircle in the curve of ε' versus ε'' [37–38]. The relationship between ε' and ε'' can be expressed by Eq. (1):

$$\left(\varepsilon' - \frac{\varepsilon_s + \varepsilon_\infty}{2}\right)^2 + (\varepsilon'')^2 = \left(\frac{\varepsilon_s - \varepsilon_\infty}{2}\right)^2 \quad (1)$$

where ε_s and ε_∞ represent the static permittivity and dielectric permittivity at the high-frequency limit. As shown in Fig. S4, there is a deformed semicircle at a low relative complex permittivity, indicating that the dielectric loss of $BaTiO_3/TiO_2$@PPy HoMSs includes various polarization losses such as interfacial polarization and dipole polarization. Besides, the Cole–Cole semicircle presents a straight line at a high relative complex permittivity, which indicates that the dielectric loss of $BaTiO_3/TiO_2$@PPy HoMSs is dominated by conduction loss.

RL value is the most intuitive parameter to evaluate EMW absorption performance. In general, the part of RL value less than −10 dB is considered to be EAB, which means 90% of EMW is absorbed. Based on transmission line theory, RL can be obtained by Eqs. (2) and (3):

$$\mathrm{RL} = 20\lg\left|\frac{Z_i - Z_o}{Z_i + Z_o}\right| = 20\lg\left|\frac{(Z_i/Z_o) - 1}{(Z_i/Z_o) + 1}\right| \quad (2)$$

$$Z_i = Z_o\sqrt{\frac{\mu_i}{\varepsilon_i}}\tanh\left(j\frac{2\pi f d}{c}\cdot\sqrt{\mu_i\varepsilon_i}\right) \quad (3)$$

where Z_i, Z_o, c, and d represent the input impedance of the absorber in air, the impedance in free space, the velocity of light, and the thickness of the absorber. In addition, ε_i and μ_i are given by $(\varepsilon' - j\varepsilon'')$ and $(\mu' - j\mu'')$, respectively [39–40].

Fig. 6(a)–(c) shows the RL curves of $BaTiO_3/TiO_2$@PPy HoMSs in the thickness range of 1–5 mm. It can be observed that $BaTiO_3/TiO_2$@PPy HoMSs have excellent EMW absorption performance. Among them, 3s-$BaTiO_3/TiO_2$@PPy has the most excellent absorbing performance, the minimum RL reaches −21.80 dB at 13.34 GHz, and the EAB is up to 4.20 GHz (13.80–18 GHz), which is higher than those of 1s- and 2s-$BaTiO_3/TiO_2$@PPy HoMSs. It is worth noting that the minimum RL value and EAB gradually shift toward low-frequency direction with the increase of absorber thickness, in-

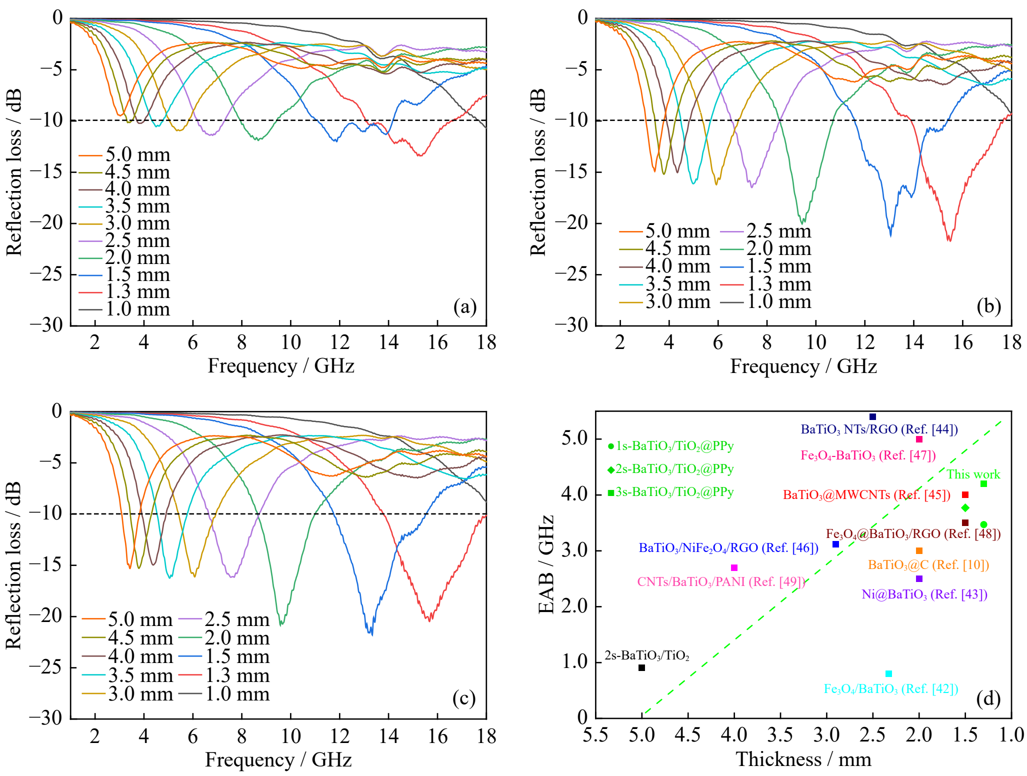

Fig. 6. RL curves of (a) 1s-$BaTiO_3/TiO_2$@PPy HoMSs, (b) 2s-$BaTiO_3/TiO_2$@PPy HoMSs, and (c) 3s-$BaTiO_3/TiO_2$@PPy HoMSs in the thickness range of 1–5 mm; (d) comparison of EAB of $BaTiO_3$-based EMW absorbing materials with different compositions and structures [10,42–49].

dicating that the thickness of $BaTiO_3/TiO_2$@PPy HoMSs can be adjusted to meet the application needs at various frequencies. This regular shifting of the peak frequency can be explained by the 1/4 wavelength formula [38,41]. Encouragingly, the optimal thickness of 3s-$BaTiO_3/TiO_2$@PPy HoMSs is only 1.3 mm, which is much smaller than those of many binary dielectric $BaTiO_3$-based composite materials (Fig. 6(d), Table S1 in supplementary information) [10,42–49].

The EMW absorption performance increases with the shell number of $BaTiO_3/TiO_2$@PPy HoMSs. This can be attributed to the increase of effective interfaces and the multiple scattering and reflection of EMW. Compared with the EMW absorbing performance of $BaTiO_3/TiO_2$ HoMSs (Fig. S5), minimum RL value and EAB of $BaTiO_3/TiO_2$@PPy HoMSs have been significantly improved. The introduction of PPy can form conductive channels inside $BaTiO_3/TiO_2$ HoMSs, and generate sufficient carriers under the external electric field to form induced current, thus accelerating the consumption of incident EMW. In addition, the multiple interfaces between PPy and $BaTiO_3/TiO_2$ are also beneficial to increase the polarization of the effective interface and accelerate the loss of EMW.

Notably, among these composites, 1s-$BaTiO_3/TiO_2$@PPy HoMSs have the strongest dielectric loss capability but the worst EMW absorption performance. RL value is determined by two crucial factors, the attenuation constant (α) and the impedance matching ratio, which describe the amplitude attenuation and the transmission probability of incident EMW in absorbers, respectively [50–51]. In general, the α value can be expressed by the following equation:

$$\alpha = \frac{\sqrt{2}\pi f}{c} \times \sqrt{(\mu''\varepsilon'' - \mu'\varepsilon') + \sqrt{(\mu''\varepsilon'' - \mu'\varepsilon')^2 + (\mu'\varepsilon'' + \mu''\varepsilon')^2}} \quad (4)$$

As shown in Fig. 7(a), the α values of $BaTiO_3/TiO_2$@PPy HoMSs are gradually enhanced in the frequency range from 1 to 18 GHz, implying that the strong attenuation mainly occurs in the high frequency range. In addition, the α value of 1s-$BaTiO_3/TiO_2$@PPy HoMSs is larger than that of 3s-$BaTiO_3/TiO_2$@PPy HoMSs, indicating that 1s-$BaTiO_3/TiO_2$@PPy has the strongest loss capability, which is consistent with the results of electrical loss.

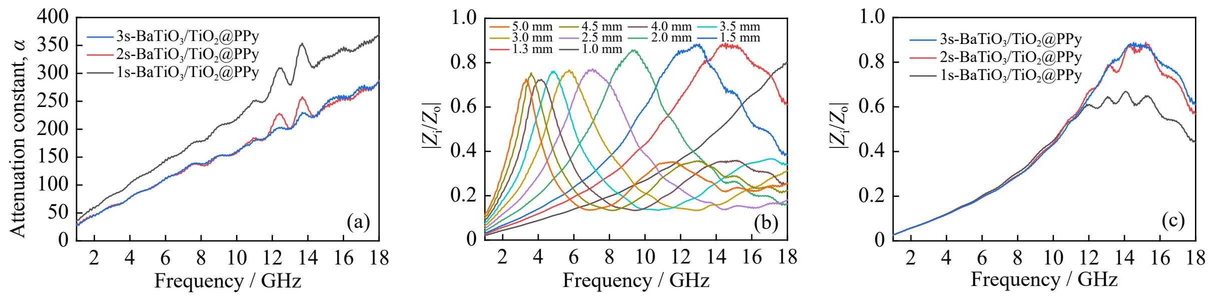

Fig. 7. (a) Attenuation constant α curves of $BaTiO_3/TiO_2$@PPy HoMSs, (b) impedance matching ratio of 3s-$BaTiO_3/TiO_2$@PPy HoMSs with thickness of 1–5 mm, and (c) impedance matching ratio curves of $BaTiO_3/TiO_2$@PPy HoMSs at the thickness of 1.3 mm.

The impedance matching ratio is the key parameter that determines the probability of EMW incident to the absorber [52]. According to the reflection coefficient Eq. (5) and Eq. (6), when $|Z_i/Z_o| = 1$, the EMW will completely enter the absorber without reflection [37,53–54].

$$R = \frac{Z_o - Z_i}{Z_o + Z_i} \quad (5)$$

$$\left|\frac{Z_i}{Z_o}\right| = \left|\sqrt{\frac{\mu_i}{\varepsilon_i}} \tanh\left(j\frac{2\pi f d}{c} \cdot \sqrt{\mu_i \varepsilon_i}\right)\right| \quad (6)$$

Fig. 7(b) exhibits the impedance matching ratio of 3s-$BaTiO_3/TiO_2$@PPy HoMSs. It can be seen that $|Z_i/Z_o|$ is closer to 1 when the absorber thickness is 1.3 mm, indicating that the incident of EMW is higher at this thickness, which is consistent with the EMW absorption performance. As shown in Fig. 7(c), although 1s-$BaTiO_3/TiO_2$@PPy has the strongest dielectric loss capability, its $|Z_i/Z_o|$ value is the lowest around 12–18 GHz, indicating its high surface reflectivity. On the contrary, 3s-$BaTiO_3/TiO_2$@PPy has moderate dielectric loss capability, but its $|Z_i/Z_o|$ value is the highest, indicating its low surface reflectivity. It can be concluded from the above results that the combination of moderate attenuation ability and impedance matching of 3s-$BaTiO_3/TiO_2$@PPy HoMSs endow them excellent EMW absorption performance.

Fig. 8 shows the schematic diagram of the EMW absorption mechanism of $BaTiO_3/TiO_2$@PPy HoMSs. Firstly, the hollow structure and the large number of intergranular pores of $BaTiO_3/TiO_2$@PPy HoMSs can effectively improve the dielectric impedance balance between the absorber and the air. Based on Maxwell-Garnett theory, the effective permittivity ($\varepsilon_{\mathrm{eff}}^{\mathrm{MG}}$) can be expressed as follows [33,55]:

$$\varepsilon_{\mathrm{eff}}^{\mathrm{MG}} = \varepsilon_1 \frac{(\varepsilon_2 + 2\varepsilon_1) + 2f_v(\varepsilon_2 - \varepsilon_1)}{(\varepsilon_2 + 2\varepsilon_1) - f_v(\varepsilon_2 - \varepsilon_1)} \quad (7)$$

where f_v, ε_1, and ε_2 represent the volume fraction of the pores and the permittivities of the solid and air, respectively. According to Eq. (7), HoMSs with large specific surface area results in large f_v, which leads to a low $\varepsilon_{\mathrm{eff}}^{\mathrm{MG}}$. The low $\varepsilon_{\mathrm{eff}}^{\mathrm{MG}}$ indicates that the incident EMW is able to penetrate more through the absorber into the interior of the HoMSs, rather than be reflected back into the environment directly. Secondly, multiple shells of HoMS, as well as the adjacent HoMSs can realize multiple scattering and reflections of EMW, thus extending the propagation distance of EMW within the absorber and enhancing the effective absorption of

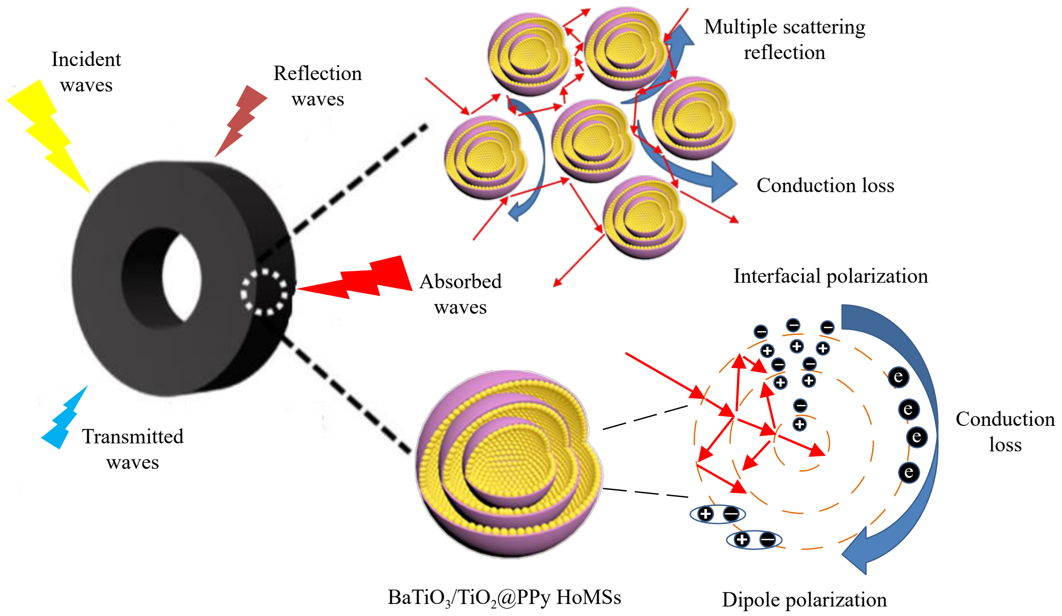

Fig. 8. Schematic diagram of EMW absorption mechanism of $BaTiO_3/TiO_2$@PPy HoMSs.

EMW. Thirdly, as the conductive polymer, PPy has a unique conjugated π bond, under the action of an external electromagnetic field, the π electrons will move directionally to form a conductive network to consume the incident EMW. Therefore, the introduction of PPy into the dielectric material $BaTiO_3/TiO_2$ HoMSs is beneficial to further improve the consumption of EMW. Fourth, after the introduction of PPy, new interfaces will be formed with $BaTiO_3/TiO_2$, which is beneficial to increase the interfacial polarization. The polar groups and defects in $BaTiO_3/TiO_2$@PPy HoMSs will become the polarization centers of dipoles, converting electromagnetic energy into thermal energy, thereby accelerating the loss of EMW. Finally, HoMSs have abundant inner surface, outer surface, and pore interface, and thus can enhance the interfacial polarization loss of EMW. In summary, the synergistic effect of various loss mechanisms confers excellent absorbing performance of $BaTiO_3/TiO_2$@PPy HoMSs.

4. Conclusion

In conclusion, we developed a facile and controllable strategy for the preparation $BaTiO_3/TiO_2$@PPy HoMSs. $BaTiO_3/TiO_2$@PPy HoMSs exhibit excellent electromagnetic wave absorption performance due to the synergistic effect of different compositions and the unique hollow multishelled configuration. In particular, the 3s-$BaTiO_3/TiO_2$@PPy HoMSs have the most excellent absorbing performance with an optimal absorber thickness of only 1.3 mm, which is superior to most of the reported $BaTiO_3$-based composite. This study suggests that multi-component complexes with hollow multishelled structures have great potential for application to high-performance wave absorbing materials.

Acknowledgements

This work was financially supported by the National Natural Science Foundation of China (Nos. 51972305, 21820102002, 21931012, 51932001, and 51872024).

Conflict of Interest

All authors have no financial/commercial conflicts of interest.

Supplementary Information

The online version contains supplementary material available at https://doi.org/10.1007/s12613-022-2556-7.

References

[1] F. Shahzad, M. Alhabeb, C.B. Hatter, *et al.*, Electromagnetic interference shielding with 2D transition metal carbides (MXenes), *Science*, 353(2016), No. 6304, p. 1137.

[2] H. Hu, G.D. Niu, Z.P. Zheng, L. Xu, L.Y. Liu, and J. Tang, Perovskite semiconductors for ionizing radiation detection, *EcoMat*, 4(2022), No. 6, art. No. e12258.

[3] Y. Li, X.F. Liu, X.Y. Nie, *et al.*, Multifunctional organic–inorganic hybrid aerogel for self-cleaning, heat-insulating, and highly efficient microwave absorbing material, *Adv. Funct. Mater.*, 29(2019), No. 10, art. No. 1807624.

[4] X.T. Chen, M. Zhou, Y. Zhao, *et al.*, Morphology control of eco-friendly chitosan-derived carbon aerogels for efficient microwave absorption at thin thickness and thermal stealth, *Green Chem.*, 24(2022), No. 13, p. 5280.

[5] F. Wang, W.H. Gu, J.B. Chen, *et al.*, The point defect and electronic structure of K doped $LaCo_{0.9}Fe_{0.1}O_3$ perovskite with enhanced microwave absorbing ability, *Nano Res.*, 15(2022), No. 4, p. 3720.

[6] X.P. Li, Z.M. Deng, Y. Li, *et al.*, Controllable synthesis of hollow microspheres with Fe@carbon dual-shells for broad bandwidth microwave absorption, *Carbon*, 147(2019), p. 172.

[7] X. Qiu, L.X. Wang, H.L. Zhu, Y.K. Guan, and Q.T. Zhang, Lightweight and efficient microwave absorbing materials based on walnut shell-derived nano-porous carbon, *Nanoscale*, 9(2017), No. 22, p. 7408.

[8] L.R. Cui, X.J. Han, F.Y. Wang, H.H. Zhao, and Y.C. Du, A re-

view on recent advances in carbon-based dielectric system for microwave absorption, *J. Mater. Sci.*, 56(2021), No. 18, p. 10782.
[9] L.X. Gai, H.H. Zhao, F.Y. Wang, *et al*., Advances in core–shell engineering of carbon-based composites for electromagnetic wave absorption, *Nano Res.*, 15(2022), No. 10, p. 9410.
[10] L.R. Cui, C.H. Tian, L.L. Tang, *et al*., Space-confined synthesis of core–shell $BaTiO_3$@carbon microspheres as a high-performance binary dielectric system for microwave absorption, *ACS Appl. Mater. Interfaces*, 11(2019), No. 34, p. 31182.
[11] L. Wang, X. Li, Q.Q. Li, Y.H. Zhao, and R.C. Che, Enhanced polarization from hollow cube-like $ZnSnO_3$ wrapped by multi-walled carbon nanotubes: As a lightweight and high-performance microwave absorber, *ACS Appl. Mater. Interfaces*, 10(2018), No. 26, p. 22602.
[12] Z.G. Mu, G.K. Wei, H. Zhang, *et al*., The dielectric behavior and efficient microwave absorption of doped nanoscale $LaMnO_3$ at elevated temperature, *Nano Res.*, 15(2022), No. 8, p. 7731.
[13] D. Mao, J.W. Wan, J.Y. Wang, and D. Wang, Sequential templating approach: A groundbreaking strategy to create hollow multishelled structures, *Adv. Mater.*, 31(2019), No. 38, art. No. 1802874.
[14] Y.Z. Wei, N.L. Yang, K.K. Huang, *et al*., Steering hollow multishelled structures in photocatalysis: Optimizing surface and mass transport, *Adv. Mater.*, 32(2020), No. 44, art. No. 2002556.
[15] Z. Zhang, D. Mao, M. Yang, and R.B. Yu, Application of hollow multi-shelled structures in electromagnetic wave field, *Chem. J. Chin. Univ.*, 42(2021), No. 5, p. 1395.
[16] L.J. Yang, H.L. Lv, M. Li, Y. zhang, J.C. Liu, and Z.H. Yang, Multiple polarization effect of shell evolution on hierarchical hollow C@MnO_2 composites and their wideband electromagnetic wave absorption properties, *Chem. Eng. J.*, 392(2020), art. No. 123666.
[17] J.W. Liu, J. Cheng, R.C. Che, J.J. Xu, M.M. Liu, and Z.W. Liu, Double-shelled yolk–shell microspheres with Fe_3O_4 cores and SnO_2 double shells as high-performance microwave absorbers, *J. Phys. Chem. C*, 117(2013), No. 1, p. 489.
[18] J.Q. Tao, J.T. Zhou, Z.J. Yao, *et al*., Multi-shell hollow porous carbon nanoparticles with excellent microwave absorption properties, *Carbon*, 172(2021), p. 542.
[19] G. Ahmad, M.B. Dickerson, Y. Cai, *et al*., Rapid bioenabled formation of ferroelectric $BaTiO_3$ at room temperature from an aqueous salt solution at near neutral pH, *J. Am. Chem. Soc.*, 130(2008), No. 1, p. 4.
[20] F. Xia, J.W. Liu, D. Gu, P.F. Zhao, J. Zhang, and R.C. Che, Microwave absorption enhancement and electron microscopy characterization of $BaTiO_3$ nano-torus, *Nanoscale*, 3(2011), No. 9, p. 3860.
[21] L.H. Tian, X.D. Yan, J.L. Xu, *et al*., Effect of hydrogenation on the microwave absorption properties of $BaTiO_3$ nanoparticles, *J. Mater. Chem. A*, 3(2015), No. 23, p. 12550.
[22] Y.F. Zhu, Q.Q. Ni, and Y.Q. Fu, One-dimensional barium titanate coated multi-walled carbon nanotube heterostructures: Synthesis and electromagnetic absorption properties, *RSC Adv.*, 5(2015), No. 5, p. 3748.
[23] S.P. Li, Y. Huang, N. Zhang, M. Zong, and P.B. Liu, Synthesis of polypyrrole decorated FeCo@SiO_2 as a high-performance electromagnetic absorption material, *J. Alloys Compd.*, 774(2019), p. 532.
[24] Z.C. Wu, D.G. Tan, K. Tian, *et al*., Facile preparation of core–shell Fe_3O_4@polypyrrole composites with superior electromagnetic wave absorption properties, *J. Phys. Chem. C*, 121(2017), No. 29, p. 15784.
[25] R. Pang, X.J. Hu, S.Y. Zhou, *et al*., Preparation of multi-shelled conductive polymer hollow microspheres by using Fe_3O_4 hollow spheres as sacrificial templates, *Chem. Commun.*, 50(2014), No. 83, p. 12493.
[26] H. Ren, R.B. Yu, J.Y. Wang, *et al*., Multishelled TiO_2 hollow microspheres as anodes with superior reversible capacity for lithium ion batteries, *Nano Lett.*, 14(2014), No. 11, p. 6679.
[27] S. Goel, A. Tyagi, A. Garg, *et al*., Microwave absorption study of composites based on CQD@$BaTiO_3$ core shell and $BaFe_{12}O_{19}$ nanoparticles, *J. Alloys Compd.*, 855(2021), art. No. 157411.
[28] N.V. Blinova, J. Stejskal, M. Trchová, J. Prokeš, and M. Omastová, Polyaniline and polypyrrole: A comparative study of the preparation, *Eur. Polym. J.*, 43(2007), No. 6, p. 2331.
[29] Y.F. Zhu, L. Zhang, T. Natsuki, Y.Q. Fu, and Q.Q. Ni, Facile synthesis of $BaTiO_3$ nanotubes and their microwave absorption properties, *ACS Appl. Mater. Interfaces*, 4(2012), No. 4, p. 2101.
[30] Y.K. Liu, Y.J. Feng, X.W. Wu, and X.G. Han, Microwave absorption properties of La doped barium titanate in X-band, *J. Alloys Compd.*, 472(2009), No. 1-2, p. 441.
[31] T.W. Wang, Z.W. Yin, Y.H. Guo, *et al*., Highly selective photocatalytic conversion of glucose on holo-symmetrically spherical three-dimensionally ordered macroporous heterojunction photonic crystal, *CCS Chem.*, (2022). DOI: 10.31635/ccschem.022.202202213
[32] Y.F. Zhu, Y.Q. Fu, T. Natsuki, and Q.Q. Ni, Fabrication and microwave absorption properties of $BaTiO_3$ nanotube/polyaniline hybrid nanomaterials, *Polym. Compos.*, 34(2013), No. 2, p. 265.
[33] P.B. Liu, S. Gao, Y. Wang, Y. Huang, Y. Wang, and J.H. Luo, Core–shell CoNi@graphitic carbon decorated on B, N-codoped hollow carbon polyhedrons toward lightweight and high-efficiency microwave attenuation, *ACS Appl. Mater. Interfaces*, 11(2019), No. 28, p. 25624.
[34] B. Zhao, W.Y. Zhao, G. Shao, B.B. Fan, and R. Zhang, Corrosive synthesis and enhanced electromagnetic absorption properties of hollow porous Ni/SnO_2 hybrids, *Dalton Trans.*, 44(2015), No. 36, p. 15984.
[35] H. Li, S.S. Bao, Y.M. Li, *et al*., Optimizing the electromagnetic wave absorption performances of designed Co_3Fe_7@C yolk–shell structures, *ACS Appl. Mater. Interfaces*, 10(2018), No. 34, p. 28839.
[36] M.M. Lu, W.Q. Cao, H.L. Shi, *et al*., Multi-wall carbon nanotubes decorated with ZnO nanocrystals: Mild solution-process synthesis and highly efficient microwave absorption properties at elevated temperature, *J. Mater. Chem. A*, 2(2014), No. 27, p. 10540.
[37] Z.H. Yang, Y. Zhang, M. Li, *et al*., Surface architecture of Ni-based metal organic framework hollow spheres for adjustable microwave absorption, *ACS Appl. Nano Mater.*, 2(2019), No. 12, p. 7888.
[38] S.Y. Wang, S.S. Peng, S.T. Zhong, and W. Jiang, Construction of SnO_2/Co_3Sn_2@C and SnO_2/Co_3Sn_2@air@C hierarchical heterostructures for efficient electromagnetic wave absorption, *J. Mater. Chem. C*, 6(2018), No. 35, p. 9465.
[39] Y. Qiu, Y. Lin, H.B. Yang, L. Wang, M.Q. Wang, and B. Wen, Hollow Ni/C microspheres derived from Ni-metal organic framework for electromagnetic wave absorption, *Chem. Eng. J.*, 383(2020), art. No. 123207.
[40] Z.N. Li, X.J. Han, Y. Ma, *et al*., MOFs-derived hollow Co/C microspheres with enhanced microwave absorption performance, *ACS Sustainable Chem. Eng.*, 6(2018), No. 7, p. 8904.
[41] G.S. Wen, X.C. Zhao, Y. Liu, H. Zhang, and C. Wang, Facile synthesis of RGO/Co@Fe@Cu hollow nanospheres with efficient broadband electromagnetic wave absorption, *Chem. Eng. J.*, 372(2019), p. 1.
[42] S.H. Choi, J.H. Oh, and T. Ko, Preparation and characteristics of Fe_3O_4-encapsulated $BaTiO_3$ powder by ultrasound-enhanced

ferrite plating, *J. Magn. Magn. Mater.*, 272-276(2004), p. 2233.
[43] G.M. Shi, Y.F. Li, L. Ai, and F.N. Shi, Two step synthesis and enhanced microwave absorption properties of polycrystalline $BaTiO_3$ coated Ni nanocomposites, *J. Alloys Compd.*, 680(2016), p. 735.
[44] J. Ran, M.J. Guo, L. Zhong, and H.Q. Fu, *In situ* growth of $BaTiO_3$ nanotube on the surface of reduced graphene oxide: A lightweight electromagnetic absorber, *J. Alloys Compd.*, 773(2019), p. 423.
[45] X. Huang, Z.R. Chen, L.F. Tong, M.N. Feng, Z.J. Pu, and X.B. Liu, Preparation and microwave absorption properties of $BaTiO_3$@MWCNTs core/shell heterostructure, *Mater. Lett.*, 111(2013), p. 24.
[46] Y. Zuo, J.H. Luo, M.L. Cheng, K. Zhang, and R.L. Dong, Synthesis, characterization and enhanced electromagnetic properties of $BaTiO_3/NiFe_2O_4$-decorated reduced graphene oxide nanosheets, *J. Alloys Compd.*, 744(2018), p. 310.
[47] Y. Huang, J.D. Ji, Y. Chen, *et al*., Broadband microwave absorption of Fe_3O_4–$BaTiO_3$ composites enhanced by interfacial polarization and impedance matching, *Composites Part B*, 163(2019), p. 598.
[48] Z. Peng, W. Jiang, Y.P. Wang, and S.T. Zhong, Synthesis and microwave absorption properties of Fe_3O_4@$BaTiO_3$/reduced graphene oxide nanocomposites, *J. Mater. Sci. Mater. Electron.*, 27(2016), No. 2, p. 1304.
[49] L.J. Yu, Y.F. Zhu, C. Qian, Q. Fu, Y.Z. Zhao, and Y.Q. Fu, Nanostructured barium titanate/carbon nanotubes incorporated polyaniline as synergistic electromagnetic wave absorbers, *J. Nanomater.*, 2016(2016), art. No. 6032307.
[50] H.L. Lv, H.Q. Zhang, J. Zhao, G.B. Ji, and Y.W. Du, Achieving excellent bandwidth absorption by a mirror growth process of magnetic porous polyhedron structures, *Nano Res.*, 9(2016), No. 6, p. 1813.
[51] Y.H. Wang, X.J. Han, P. Xu, *et al*., Synthesis of pomegranate-like Mo_2C@C nanospheres for highly efficient microwave absorption, *Chem. Eng. J.*, 372(2019), p. 312.
[52] W.Y. Dai, F. Chen, H. Luo, *et al*., Synthesis of yolk–shell structured carbonyl iron@void@nitrogen doped carbon for enhanced microwave absorption performance, *J. Alloys Compd.*, 812(2020), art. No. 152083.
[53] J. Ouyang, Z.L. He, Y. Zhang, H.M. Yang, and Q.H. Zhao, Trimetallic FeCoNi@C nanocomposite hollow spheres derived from metal-organic frameworks with superior electromagnetic wave absorption ability, *ACS Appl. Mater. Interfaces*, 11(2019), No. 42, p. 39304.
[54] B. Qu, C.L. Zhu, C.Y. Li, X.T. Zhang, and Y.J. Chen, Coupling hollow Fe_3O_4–Fe nanoparticles with graphene sheets for high-performance electromagnetic wave absorbing material, *ACS Appl. Mater. Interfaces*, 8(2016), No. 6, p. 3730.
[55] B. Zhao, X.Q. Guo, W.Y. Zhao, *et al*., Facile synthesis of yolk–shell Ni@void@SnO_2(Ni_3Sn_2) ternary composites via galvanic replacement/Kirkendall effect and their enhanced microwave absorption properties, *Nano Res.*, 10(2017), No. 1, p. 331.